ACS OMEGA

http://pubs.acs.org/journal/acsodf

Article

Narrowband Polaritonic Thermal Emitters Driven by Waste Heat

Guanyu Lu, Joshua Ryan Nolen, Thomas G. Folland, Marko J. Tadjer, Don Greg Walker, and Joshua D. Caldwell*

Cite This: *ACS Omega* 2020, 5, 10900−10908

Read Online

ACCESS | Metrics & More | Article Recommendations | Supporting Information

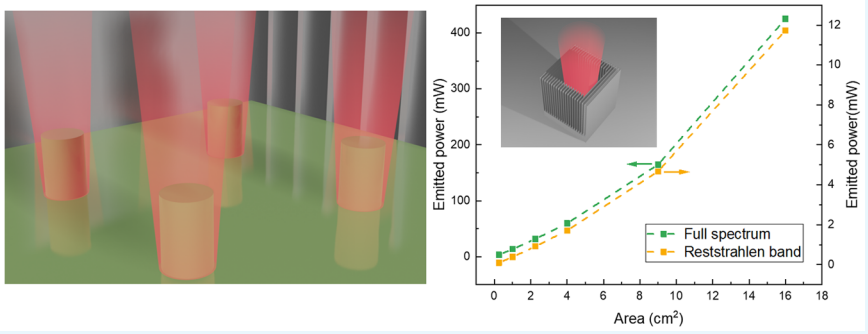

ABSTRACT: There are a broad range of applications for narrowband long-wave infrared (LWIR) sources, especially within the 8−12 μm atmospheric window. These include infrared beacons, free-space communications, spectroscopy, and potentially on-chip photonics. Unfortunately, commercial light-emitting diode (LED) sources are not available within the LWIR, leaving only gas-phase and quantum cascade lasers, which exhibit low wall-plug efficiencies and in many cases require large footprints, precluding their use for many applications. Recent advances in nanophotonics have demonstrated the potential for tailoring thermal emission into an LED-like response, featuring narrowband, polarized thermal emitters. In this work, we demonstrate that such nanophotonic IR emitting metamaterials (NIREMs), featuring near-unity absorption, can serve as LWIR sources with effectively no net power consumption, enabling their operation entirely by waste heat from conventional electronics. Using experimental emissivity spectra from a SiC NIREM device in concert with a thermodynamic compact model, we verify this feasibility for two test cases: a NIREM device driven by waste heat from a CPU heat sink and one operating using a low-power resistive heater for elevated temperature operation. To validate these calculations, we experimentally determine the temperature-dependent NIREM irradiance and the angular radiation pattern. We purport that these results provide a first proof-of-concept for waste heat-driven thermal emitters potentially employable in a variety of infrared application spaces.

INTRODUCTION

As defined by Planck's blackbody radiation law, heat radiated from near-room temperature objects emits within the long-wave infrared (LWIR), with room temperature (298 K) corresponding to a peak Wien wavelength of 9.72 μm. Such thermal radiation is the basis of incandescent light sources and of thermal imaging schemes while more recently, it has also been exploited for concepts such as passive radiative cooling[1,2] and increased radiative heat transfer rates at nanoscale separations.[3,4] The broadband emission patterns provided by traditional blackbody thermal emitters are advantageous in applications such as ambient lighting and Fourier transform infrared (FTIR) spectroscopy. However, the broadband, unpolarized, and omnidirectional nature of the emission is less useful for many applications, such as nondispersive IR gas sensors[5] or free-space optical communications.[6] For these applications, there are essentially three highly desirable properties: (1) a high degree of spatial coherence (aka directed emission), (2) narrow emitted frequency bandwidth, and (3) sufficient emitted power (several 10's of mW). Past work has shown that many of these requirements can be met by polaritonic antennas.[7−9] Here, we illustrate that such emitters can be produced at a large scale, with the efficiency necessary to be driven at relatively low temperatures by harnessing waste heat. Further, we experimentally determine the spectral irradiance and angular radiation patterns from such nanophotonic IR emitting metamaterial (NIREM) devices, demonstrating quantitative agreement with thermodynamic modeling. Based on these results, we validate our theoretical model illustrating the potential for driving these devices using

Received: February 10, 2020
Accepted: April 22, 2020
Published: May 5, 2020

only waste heat, offering potential avenues for LWIR emitters capable of operating in remote locations with minimal power.

The NIREM devices at the heart of this work offer technological significance based on the current lack of competitive light-emitting diode (LED)-like sources available within the LWIR. In this spectral range, such narrowband, polarized, and coherent sources exist in the form of gas lasers (e.g., CO_2 laser) and quantum cascade lasers. However, the former has an exceptionally large footprint while both laser types exhibit low wall-plug efficiencies, especially when lower optical power is required. The associated high-power consumption precludes the implementation of such LWIR lasers for applications such as on-chip photonics or in autonomous systems where power and weight restrictions would limit their usage.[10,11] Although the proposed NIREM devices do not provide temporally coherent light because of the incoherent nature of thermal emission, they do potentially offer narrow spectral bandwidths and polarized emission appropriate for most applications where LEDs would be sufficient. Further, methodologies for inducing periodicity have been established.[7,12,13] Therefore, finding alternative solutions for realizing a low-power, LED-like emission in the LWIR is of distinct interest in both commercial and defense sectors.

Previous studies have shown that narrowband thermal emission can be achieved using photonic crystals,[14] but these require extensive device sizes in comparison to the mode volume where emission is generated. Further, these mode properties are strongly angle-dependent. However, advances in nanophotonics have demonstrated the potential for realizing narrowband,[9] spatially coherent,[7] and polarized emission[8,9] through the thermal excitation of surface polaritons as an alternative solution. Polaritons are quasiparticles comprising a photon and a coherently oscillating charge. There are a variety of different forms of polaritons,[15−17] with surface plasmon polaritons (SPPs) providing the most broadly investigated type, with IR thermal emitters having been reported through the implementation of the so-called perfect absorber geometry[18] and by implementing Berreman modes[19] within ultrathin polaritonic films.[20] In this work, we focus on surface phonon polaritons (SPhPs[21,22]), where the charge is in the form of the oscillating ionic charges on a polar crystal lattice, here 4H−SiC. Such quasiparticles are the basis for the prior reports of polarized, narrowband, and thermal emitters realized in periodic arrays of nanoantennas that support localized SPhPs[9] while such materials have also been used for the realization of an alternative concept for narrowband, near-unity emissivity through lossy Huygen's mode approach.[23] Because of the long scattering lifetimes of optic phonons, SPhPs exhibit significantly reduced optical losses when compared to SPPs[22] with an emission frequency that can be tuned throughout the reststrahlen band of the material, which is bound by the transverse (TO) and longitudinal optic (LO) phonons. Ideally, it would be preferable if one could realize such LWIR light sources that could be driven only by waste heat or low-power electronic circuits to expand their potential applications and operational uses. Our calculations imply that devices offering sufficient spectral irradiance can indeed be driven entirely by waste heat extracted even from low-temperature sources, such as the heat sink of a common CPU. This is despite the typical limited thermal budget of such devices and thus offers emitter functionality without risking the functional integrity of the CPU. This approach is also shown to be equally valid for alternative higher temperature heat sources, such as combustion engines. Our reported thermodynamic model is validated by direct measurements of the spectral irradiance of our NIREM device, therefore offering strong credibility to the reported predictions.

RESULTS AND DISCUSSION

Waste Heat-Driven NIREM. For polar materials, such as SiC, the coherent vibrations of the lattice (optic phonons) result in a net dipole moment, leading to the strong absorption of light at the TO phonon frequency, and a corresponding breaking of the degeneracy of the optic phonons at the γ point, causing the LO phonon to shift to higher frequencies.[24] It is within the reststrahlen band that SPhPs may be stimulated, resulting in highly confined optical fields supported at the boundary between the polar crystal and a dielectric (typically air). The lower optical loss of SPhPs[22] results in substantially reduced resonance linewidths,[25−27] which are ideal for narrowband emitter applications.[28] These highly absorptive, yet narrowband, localized SPhP resonances offer significant potential for proposed LED-like radiation achievable with such NIREM devices.

Our hypothesis is that we can replace a significant portion of a CPU heat sink (Figure 1a) with a SiC NIREM device (Figure 1b), and the NIREM could be operated using the waste heat generated by the CPU without significantly influencing the device operational temperature. To test this concept, we considered the analysis of a canonical 100 W CPU and restrict the operation to a maximum temperature of 85 °C, with the commercial heat sink exposed to 25 °C ambient air. A SiC-based NIREM of variable area was placed at the center of a typical 36 cm^2 heat sink. The heat-transfer analysis (discussed below) involves a lumped model, incorporating the thermal transport and radiative heat transfer of the CPU, heat sink, NIREM, and interfacial junctions, as well as incorporating

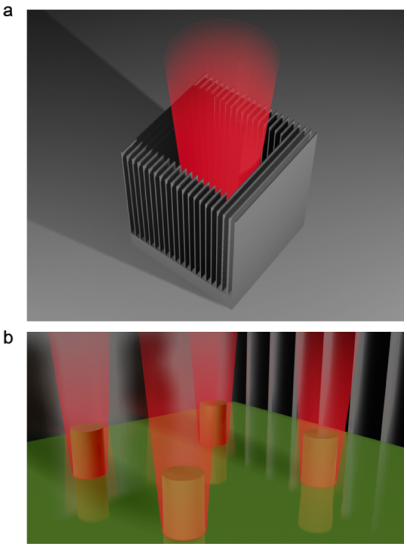

Figure 1. Schematic of the thermal design by replacing a portion of the CPU heat sink with an embedded NIREM device: (a) The center portion of the commercial heat sink is replaced with a SiC-based NIREM, which is heated up by the waste heat from a canonical CPU and acted as the IR source, and (b) fabricated SiC pillars with the substrate (transparent green) are located on top of the center of the heat sink (not to scale), with artistically showing the IR beam from the SiC thermal emitter.

https://dx.doi.org/10.1021/acsomega.0c00600
ACS Omega 2020, 5, 10900−10908

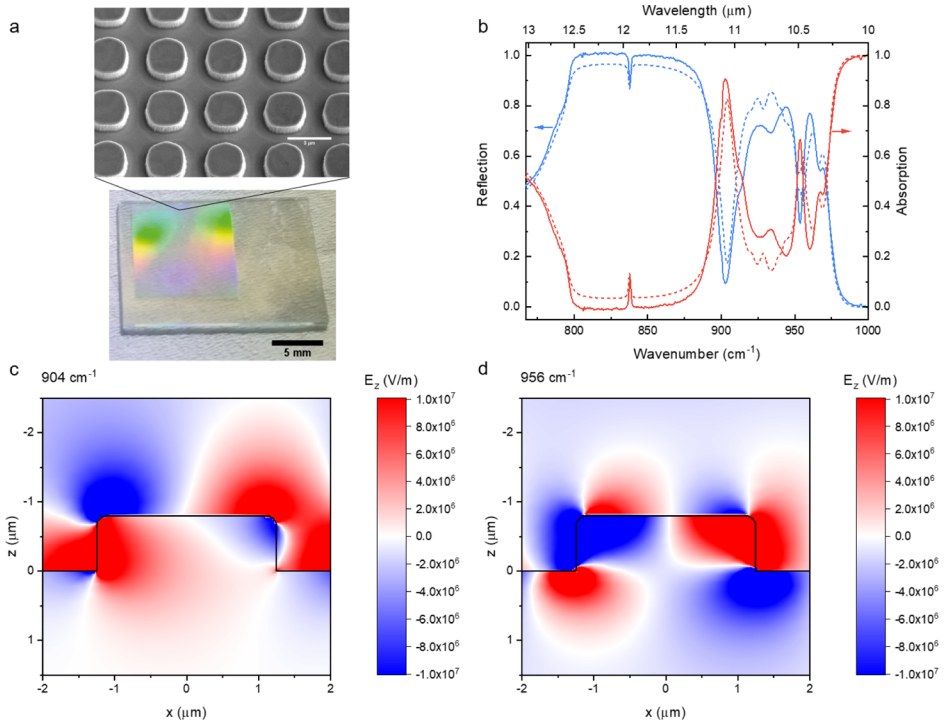

Figure 2. (a) Optical and SEM image of the large area SiC array sample (scale bar of SEM image: 3 μm), (b) experimental and simulated reflection and absorption spectra of the large-scale SiC array sample (solid lines: experimental results; dashed: simulated results), (c) field profile of the simulated structure at 904 cm^{-1}, and (d) field profile of the simulated structure at 956 cm^{-1}.

necessary convection effects that drive the heat sink cooling, and thus will influence the radiative emission from the NIREM device. Using the experimental spectral emissivity measured from our fabricated SiC NIREM structure (discussed below), we calculate the surface temperature and emitted power as a function of the heat sink surface area, with the goal of determining how much of the heat sink surface can be reasonably replaced with a NIREM device without the CPU, surpassing the maximum operating temperature.

Optimization of NIREM Design for Near-Unity Absorption. In an effort to test our concept, we fabricated a large-area SiC nanopillar array (approximately 1 cm by 1 cm array size) using optical lithography and reactive ion etching,[29] with the resonant structure optimized using three-dimensional electromagnetic simulations to achieve maximum absorption while maintaining a narrow spectral linewidth. Near-unity absorption is desirable, as through Kirchhoff's law, and this implies near-unity emissivity, with the same angular and frequency dependences. Previous studies[25,27] have shown that two primary localized SPhP modes are supported in cylindrical nanopillars fabricated into a semi-insulating 4H−SiC substrate. These are the monopole mode, which is a modified longitudinal dipole,[25] and the transverse dipole modes. Here, the close spectral proximity of these two modes results in near-unity absorption, with the design exploiting this modal overlap serving as the basis for the large-scale 4H−SiC NIREM devices we fabricated. Fabrication details can be found in the Methods. The overall fabricated structure is shown in the optical and scanning electron microscopy (SEM) images provided in Figure 2a, with the SiC nanopillar diameter of 2.5 μm, height of 0.8 μm, and the center-to-center pitch of 4 μm. To extract the absorption spectra of this structure over the spectral range of interest for our thermodynamic model (4−20 μm free-space wavelengths), we collected reflection and transmission spectra from this large-area 4H−SiC array using a Hyperion 2000 IR microscope attached to a Bruker Vertex 70v FTIR spectrometer. Ignoring the contribution of scattering, the absorption can be determined by $A(\omega) = 1 - R(\omega) - T(\omega)$, where A, R, and T are the frequency-dependent absorption, reflection, and transmission from the nanopillar array. We observed two strong resonances (solid lines in Figure 2b), with the strongest at 903 cm^{-1} corresponding to near 90% absorption and another resonance near at 954 cm^{-1}.

To understand the origin of these two strong absorptive modes, we performed finite element method (FEM) simulations using CST Microwave Studio for the fabricated structure. The simulated reflection and absorption spectra (dashed lines in Figure 2b, average of p- and s-polarized spectra to mimic the unpolarized light with the incident angle of 18° used in experiments) exhibit these two strong resonances, with near-unity absorption observed for the mode at 904 cm^{-1}. The simulated electric field (E_z) at 904 cm^{-1} (Figure 2c) is indicative of a hybrid mode comprised of spectrally overlapping monopole and transverse dipole resonances. The electric field of the other strongly absorbing mode at 956 cm^{-1} (Figure 2d) is more consistent with that of a pure transverse dipole mode. Moreover, both experimental and simulated spectra show the near-unity absorption with linewidths as narrow as 15 cm^{-1} ($Q = \omega_{res}/\Delta\omega \approx 60$), illustrating relatively narrow, near-unity absorption, even within structures fabricated using only optical lithography. We also note that similar structures fabricated using photolithography have achieved Q factors over 90.[30]

As dictated by Kirchhoff's law, such strong narrowband absorption is also directly correlated with similar thermal emission peaks for the same NIREM device as shown in the emissivity spectra measured at different temperatures (Figure 3a). These spectra are normalized to the near-blackbody

https://dx.doi.org/10.1021/acsomega.0c00600
ACS Omega 2020, 5, 10900−10908

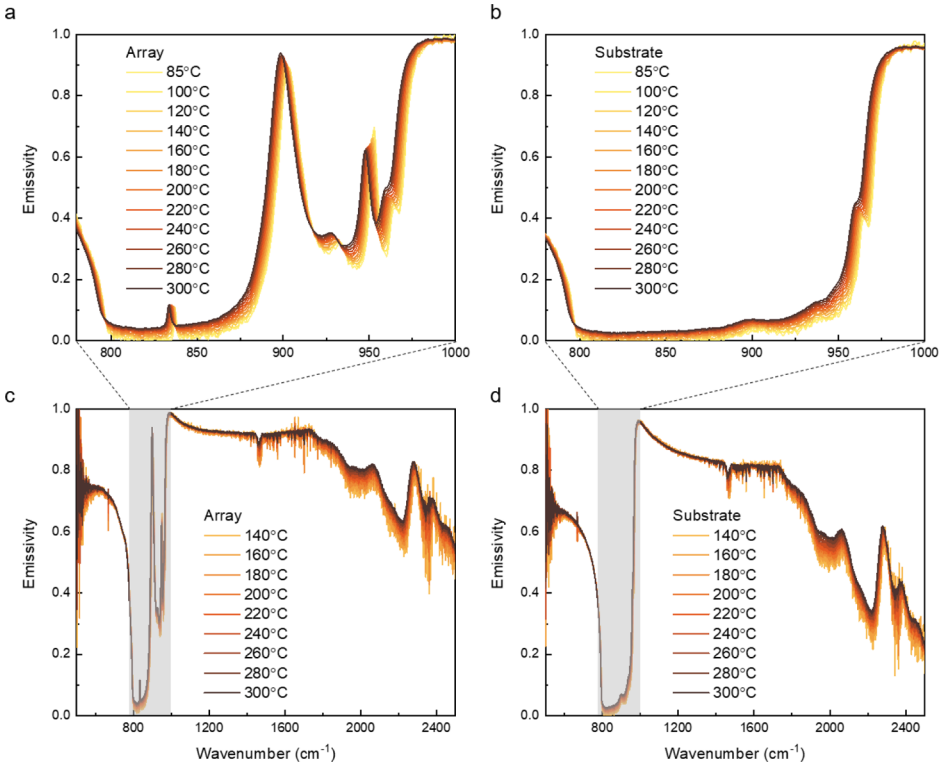

Figure 3. Temperature-dependent thermal emission measurements of the SiC NIREM device (a,c) and the SiC substrate (b,d).

radiation from an array of vertically aligned carbon nanotubes (VACNTs, with an emissivity $\epsilon \approx 0.97$[31]) at each of these temperatures (see Methods). Within the reststrahlen band, the thermal emission spectra exhibit the same two resonant peaks, with only a small spectral red-shift induced with increasing temperature, consistent with prior results.[9] This red-shift is because of the corresponding 4H−SiC thermal expansion, which also induces TO/LO phonon shifts observed from the bulk phonons in the SiC substrate (Figure 3b). The TO/LO phonon shifts are also confirmed by the reflection measurements of the SiC substrate at elevated temperatures (Figure S1). We should note that the emissivity of 4H−SiC outside of the reststrahlen band is also temperature-dependent (Figure 3c,d), with the strongest modifications occurring at frequencies above that of the LO phonon. This temperature-dependent emissivity is included in the calculated emitted power from our NIREM device.

Thermal Model of NIREM Devices Driven by Waste Heat. With the potential for narrowband, near-unity, and LED-like thermal emission demonstrated, we now turn our focus to validating the potential for driving the NIREM emission using only waste heat from a CPU. As the NIREM irradiance is directly proportional to the number of emitters (e.g., SiC nanopillars), ideally the entirety of the CPU heat sink would be replaced with our NIREM. However, as the CPU must be maintained at a safe operating temperature (here defined as 85 °C), we developed a thermal model for this NIREM/CPU/heat sink system with the goal of determining the maximum heat sink area that can be replaced by the NIREM while still maintaining the CPU below the designated safe operational temperature.

A one-dimensional model provides the relevant physics and corresponding trends to determine whether a NIREM device could be designed to scavenge heat from a chip-cooling application. In reality, the temperature gradients will adjust the results slightly. To justify the one-dimensional model we employ, however, we have provided a two-dimensional model in the Supporting Information to estimate the impact of the anticipated temperature gradients across the chip surface and heat spreader. We found that the change in temperature is negligible and thus justifying the one-dimensional approximation. The 1D model includes the thermal output of the CPU being dissipated through a heat sink (fin/fan system) with an integrated NIREM that occupies a portion of the area located at the center of the sink (Figure 1). The thermal emission of the NIREM is calculated as

$$q_n = \varepsilon_{eff}\sigma A_n(T_{chip}{}^4 - T_{surr}{}^4) \quad (1)$$

where A_n designates the area of the NIREM, σ is the Stefan−Boltzmann constant, T_{chip} is the temperature of CPU, T_{surr} is the temperature of the surrounding environment, and the effective emissivity of the device, ε_{eff}, is calculated from the measured spectral emissivity ($\varepsilon_{\lambda,T}$) as

$$\varepsilon_{eff}(T) = \frac{\int_{\lambda_1}^{\lambda_2} \varepsilon_{\lambda,T} E_b(\lambda, T)\mathrm{d}\lambda}{\int_0^{\infty} E_b(\lambda, T)\mathrm{d}\lambda} \quad (2)$$

Here, $E_b(\lambda,T)$ is the spectral irradiance of the blackbody, with λ_1 and λ_2 being the spectral bounds that bracket the reststrahlen band of SiC (~10.3−12.5 μm). However, the integral in the denominator extends from 0 to infinity, in practice, this was limited to free-space wavelengths of 20 and 4 μm (experimental data collected within this range), respectively, as outside of these bounds, the thermal emission was <8.6% of the total spectral irradiance (below 85 °C) and thus has a negligible impact upon the total emissivity. We utilize a canonical heat sink to dissipate the thermal energy from the

https://dx.doi.org/10.1021/acsomega.0c00600
ACS Omega 2020, 5, 10900−10908

CPU with any portion of the heat sink replaced by the NIREM, resulting in a decrease in heat dissipation and thus an increase in CPU temperature. To estimate the effect of the NIREM on the chip-cooling demands, we have designed a fin system that is $A_{sink} = L_f^2 = 6 \times 6$ cm^2 in area with $l_f = 6$ cm tall fins, consistent with commercial heat sink systems. We assume that a fan system provides air cooling such that the Nusselt number $Nu = 7.54$ is a constant for fully developed laminar flow between closely spaced parallel plates. This obscures the details of the flow but provides an upper bound for the load on the fin/fan system. Consequently, our results for the amount of energy scavenged by the NIREM should be considered a lower bound (as a larger area of the sink could be replaced). For our analysis, the fin thickness and the fin spacing were defined as $t_f = 0.5$ mm and $p_f = 3$ mm, respectively. The heat removal can then be calculated as

$$q_{sink} = h(\eta_f A_f + A_{sink} - N_f t_f L_f)(T_{chip} - T_{surr}) \quad (3)$$

where $N_f = L_f/p_f$ is the number of fins, T_{chip} is the temperature of the CPU, and T_{surr} is the temperature of surrounding air. The fin cooling efficiency is calculated as $\eta_f = \tanh(ml_f)/(ml_f)$, where $m = \sqrt{2h/kl_f}$, and $h = Nuk/t_f$. The thermal conductivity (k) included is that of air. Now an energy balance on the chip

$$q_{chip} = q_{sink} + q_n \quad (4)$$

can be used to calculate the resultant steady-state chip temperature, assuming a 100 W power dissipation. Additional heat loss mechanisms such as conduction through the BGA are neglected as in most applications, the heat sink acts as the dominant cooling mechanism. Furthermore, by excluding other loss mechanisms, the calculated load is maximized, and the results for the amount of energy scavenged by the NIREM should be considered a lower bound (as a larger area of the sink could be replaced).

Based on the previously measured spectral emissivity and using the aforementioned thermodynamic compact model, we calculate heat loads as a function of heat sink surface area, with the goal to determine the extent of the heat sink that can reasonably be replaced with the NIREM device without impacting the thermal management of the CPU. As stated above, as the area of the NIREM increases, the chip cooling is compromised, and thus consequently, the chip surface temperature becomes elevated (Figure 4a). Although such increases in temperature infer that more emitted power can be realized from the NIREM device (Figure 4b), extremely high temperatures are detrimental to chip operation. However, based on our calculations, the CPU can be maintained at a temperature below the designated safe upper limit (<85 °C, which is typical in most cases) during the steady state, and 100 W operation, even if nearly half of the heat sink area (16 cm^2), is replaced with a NIREM device at the center of the sink. Further, we estimate that this safe-replacement area could be significantly increased if the NIREM devices are located around the periphery of the CPU, which would be typical of a photonic interconnect configuration. This estimation is based on the fact it would not necessarily require the removal of any part of the heat sink, presuming that the purpose is to emit light parallel to the surface of the circuit board. More importantly, our analysis indicates that a NIREM device can scavenge and convert waste heat from the CPU to produce enough emitted power to drive LWIR photonic interconnects. We calculate that emitted powers on the order of 10 mW could

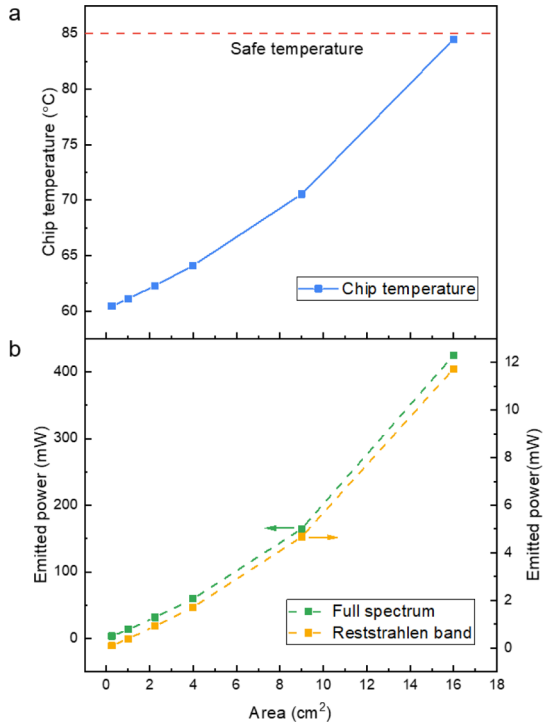

Figure 4. (a) Calculated chip temperature as a function of the area of heat sink that is replaced with the NIREM and (b) Calculated emitted power as a function of the area of heat sink that is replaced with the NIREM.

be achieved from the NIREM within the spectral region defined by the reststrahlen band of SiC (Figure 4b), under this waste heat energy-harvesting approach, even with the maximum temperature limited to 85 °C. We contend that 10 mW emitted power is especially significant considering that only thermal emission at frequencies within the spectral range, where SPhPs are supported, was considered. Thus, despite this severe restriction on the spectral window and the relatively low operating temperature, sufficient power output is indeed possible. A much higher emitted power can be achieved using the same kind of SiC NIREM design if it is mounted on a larger heat source, such as a low-power resistive heater or other high-temperature surfaces.

Direct Power Measurements of the NIREM. To determine the actual irradiance emitted from our NIREM device at a given temperature and to validate our thermodynamic model, a thermopile detector was used to directly measure the emitted power from the NIREM device. This was performed outside of the interferometer, therefore providing the integrated irradiance at all frequencies as a function of operating temperature. As a control to verify our model, we also performed these measurements on the VACNT blackbody sample. The samples were heated to temperatures ranging from 80 to 360 °C using a Linkam heating stage. Between the thermopile and the sample, there is a 5 mm by 5 mm aperture made of aluminum foil, which limits the collection area and thus provides a well-defined aperture for comparison to the theory. In order to obtain the irradiance of the NIREM, we used the Stefan−Boltzmann law to extract the view factor in our optical system, by fitting our temperature dependence as follows

https://dx.doi.org/10.1021/acsomega.0c00600
ACS Omega 2020, 5, 10900−10908

$$\frac{P}{A\sigma} = F(T_{\mathrm{VACNT}}{}^4 - T_{\mathrm{detector}}{}^4) \quad (5)$$

where P is the measured emitted power from VACNT, A is the size of the window, σ is the Stefan−Boltzmann constant, F is the view factor, and T_{VACNT} and T_{detector} are the temperatures of the VACNT and detector, respectively. After the fitting (Figure 5a), we extracted a view factor of 0.01776 ± 0.00010 and the temperature of the detector of 295.6 ± 1.8 K/22.5 ± 1.8 °C (R-square of the fitting is 0.99956). With the fitting results, the irradiance of the NIREM and unpatterned SiC substrate integrated over all frequencies is obtained using $\frac{P_{\mathrm{sample}}}{\mathrm{AF}} \frac{T_{\mathrm{sample}}{}^4}{(T_{\mathrm{sample}}{}^4 - T_{\mathrm{detector}}^4)}$, where P_{sample} is the measured emitted power from the sample, and T_{sample} is the temperature of the sample. As anticipated, the measured irradiance from the NIREM is higher than that of the SiC substrate at all measured temperatures (Figure 5b), consistent with the NIREM, providing the same background emissivity outside of the reststrahlen band but with the additional contribution from the narrowband SPhP resonances. The measured irradiance at different temperatures is compared with the calculated irradiance using eqs 1 and 2 in our thermodynamic model. In the calculations, the effective emissivity integrated at all frequencies (in practice, 4−20 μm) is calculated (inset of Figure 5c) using the measured emissivity spectra (Figure 3c,d). For both the NIREM and unpatterned SiC substrate, the measured irradiance is in excellent quantitative agreement with the calculated values and trends, which confirms our model. As such, this provides the necessary validation of our results indicating that the NIREM can indeed be driven by waste heat under our proposed approach. Considering that the emitted power is completely driven by rejected heat, these SiC NIREM devices, therefore, offer promise to operate with zero-to-low power consumption with no external power requirements for potential implementation within applications centered around on-chip photonics, IR beacons, or IR emitters for atmospheric, environmental, or chemical sensing applications.

However, above, we describe the excellent agreement between our measured and calculated integrated irradiance, as the operation of the NIREM device is centered around the thermal emission from the narrowband SPhP resonances within the reststrahlen band, and we now extend our experimental efforts to probe the spectral irradiance within this spectral range. Using the temperature-dependent emissivity within the reststrahlen band (inset of Figure 5d) defined as the ratio between the integrated emissivity of the SiC NIREM within the reststrahlen band to that of the blackbody over the entire collected spectral range (eq 2). The measured irradiance of the NIREM within the reststrahlen band at different temperatures can be obtained by employing this emissivity ratio and the direct power measurements of the blackbody sample (VACNT). With the calibrated irradiance of the NIREM in the reststrahlen band, we find that our measurements once again agree quite well with our calculated irradiance using eq 1 (Figure 5c).

Angular Radiation Pattern of the NIREM. Following our demonstration that the NIREM is applicable for on-chip photonic applications driven by waste heat, we present the angular emission profile for investigation of the spatial coherence of the emitted mode. Angle-dependent thermal emission spectra are collected using a home-made heating rotation stage (see Methods), and the two strong absorption

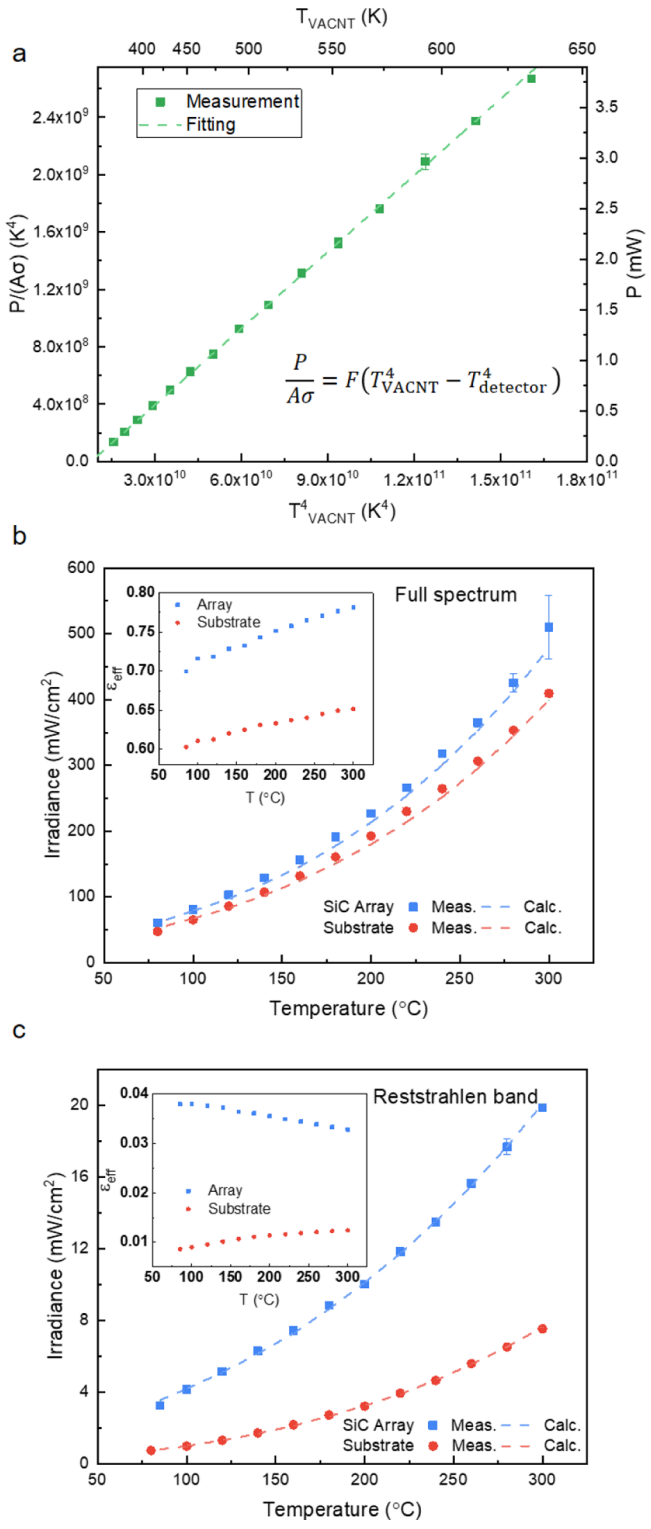

Figure 5. (a) Linear fitting of VACNT data to extract the view factor in our optical system, (b) measured and calculated irradiance of the NIREM device in the full spectrum (inset: the effective emissivity in the full spectrum), and (c) measured and calculated irradiance of the NIREM device in the reststrahlen band (inset: the effective emissivity in the reststrahlen band).

modes (898 and 948 cm^{-1}) are clear in the spectral dispersion plots (Figure 6a,c), where we present the surface plots compiled from the angle-dependent polarized thermal emission spectra. Interestingly, we can see the near-unity

https://dx.doi.org/10.1021/acsomega.0c00600
ACS Omega 2020, 5, 10900−10908

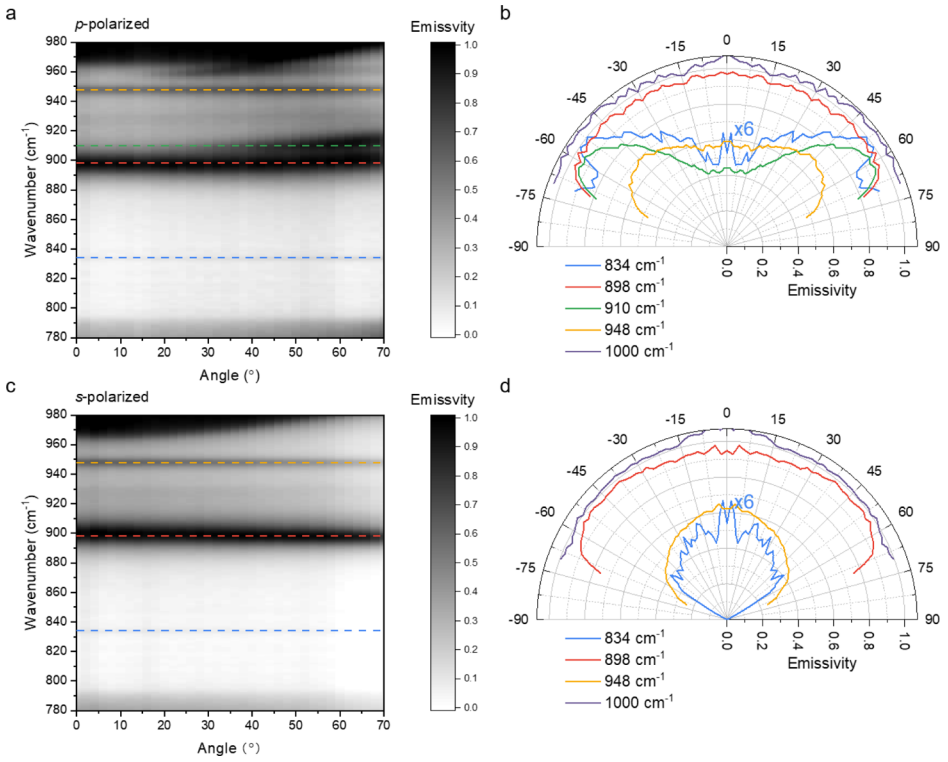

Figure 6. (a) Dispersion plot of the large-area SiC array, which is made of p-polarized angular thermal emission spectra, (b) p-polarized radiation pattern of the large-area SiC array at the frequencies showing in Figure 6a together of the frequency outside of the reststrahlen band (1000 cm^{-1}), (c) dispersion plot of the large-area SiC array, which is made of s-polarized angular thermal emission spectra, (d) s-polarized radiation pattern the large-area SiC array at the frequencies showing in Figure 6c together of the frequency outside of the reststrahlen band (1000 cm^{-1}).

absorption resonance splits into two modes at high angles in the p-polarized (Figure 6a) and unpolarized cases (Figure S4a). The mode splitting also provides further evidence that the near-unity absorption is the result of a hybrid mode comprised of at least two distinct, overlapping resonances.

From the dispersion plots, we can extract the radiation patterns of the NIREM at certain frequencies both for polarized (Figure 6b,d) and unpolarized emissions (Figure S4b). When compared to the thermal emission at a frequency outside of the reststrahlen band (1000 cm^{-1}), which has a broad distribution in the spatial domain, the two strong absorption modes (898 and 948 cm^{-1}) exhibit increases in the directionality as determined from the radiation pattern for p-polarized emission (Figure 6b). More specifically, the p-polarized emission from the resonance mode centered at 910 cm^{-1} splits from the near-unity resonance and becomes more spatially coherent. We also plot the radiation pattern of the emission resulting from the zone-folded LO phonon mode of 4H−SiC[32] (834 cm^{-1}), which exhibits a similar radiation pattern to that of the resonant modes occurring at 910 cm^{-1} while the mode at 898 cm^{-1} appears to emit into a hemisphere. We should note the directional thermal emission of the NIREM is not highly spatially coherent emission, and thus, for such devices to be potential solutions for free-space communications or interchip photonic interconnects, and additional work coupling the emitted light into a single spatial mode must be undertaken.[6,12]

CONCLUSIONS

In this work, we demonstrated that a low-power consumption, narrowband polaritonic thermal emitter can be realized and potentially driven by waste heat alone. Thus, we demonstrate that such a device is feasible even for a highly restrictive case whereby the NIREM is driven exclusively by harvesting rejected heat from a standard heat sink and 100 W CPU chip operating at temperatures below 85 °C. Using experimental emissivity spectra collected from a large-area SiC NIREM thermal emitter with near-unity absorption from one of the localized SPhP resonances in concert with a thermodynamic compact model, we demonstrate that our device can replace up to 16 cm^2 of a 36 cm^2 area heat sink, when the NIREM is located at the center of the sink. Such a device can provide in excess of 10 mW of LWIR power from the narrowband localized SPhP modes within the 10.3−12.5 μm reststrahlen band of SiC. This can be realized despite the limited thermal budget of the CPU and without risking its thermal integrity. However, for alternative application spaces where higher temperatures are more readily accessible, significant increases in the irradiance at the NIREM resonant frequencies can be achieved, with the increased power consistent with Planck's blackbody radiation law. We provide direct measurements of the irradiance from this device over both the full-detected infrared spectral range and from the SPhP resonant modes within the reststrahlen band. In all cases, excellent quantitative agreement with our thermal model was realized, offering strong validation of our calculated power outputs within this waste heat-driven NIREM concept. Based on the results reported here, we purport that waste heat-driven NIREMs could offer low size, weight, and cost, for a narrowband, and potentially polarized and spatially coherent LWIR source, even under highly restrictive thermal budgets. As such, we believe these devices could offer substantial benefits for spectroscopy performed using autonomous vehicles, as IR

https://dx.doi.org/10.1021/acsomega.0c00600
ACS Omega 2020, 5, 10900−10908

beacons or for sources appropriate for free-space communications.

METHODS

Device Fabrication. The large-scale NIREM device is fabricated by SiC dry etch and standard contact lithography processes. The SiC substrate was seeded with a thin layer of Cr/Au, upon which the NIREM device geometry was patterned using a standard positive photoresist. The as-patterned wafer was then electroplated with an approximately 1 μm thick Ni etch mask. The photoresist was then cleaned in acetone, and the exposed Cr/Au seed was removed by means of an Ar ion mill plasma process. The SiC vertical NIREM structures were then etched at a rate of about 120 nm/min in an inductively coupled plasma (ICP) reactor using a combination of SF_6/O_2 chemistry optimized to yield the nearly vertical sidewall etch profile. Details of the SiC etch process have been reported elsewhere.[29]

Numerical Simulations. FEM simulations were performed in CST studio suite 2018 using the structure mentioned before with round edges at the top of the pillars (to mimic the imperfection of fabrication, see Figure S5). The unit cell boundary conditions and a perfectly matched layer for the substrate are used in the simulations. The dielectric function used for 4H−SiC was derived from that presented in ref 33.

Optical Characterization. The room-temperature reflection and transmission spectra for the large-area 4H−SiC array sample are collected using a Hyperion 2000 IR microscope attached to a Bruker Vertex 70v FTIR spectrometer with a liquid-nitrogen-cooled HgCdTe (MCT) detector. The microscope objective used is a 15× Cassegrain objective (Pike Technologies), which illuminates the sample with an average incident angle of 18°.

Temperature-dependent Thermal Emission and Reflection Measurements. For the temperature-dependent thermal emission/reflection measurements, a heating stage with a KBr window (Linkam FTIR600) was added to the FTIR microscope, and the thermal emission/reflection spectra are measured via the 15× Cassegrain objective. To compare the reflection spectra at elevated temperatures (Figure S1), the room-temperature reflection spectrum is also collected when the sample is mounted on the heating stage with the KBr window.

Angular Thermal Emission Measurements. A custom-built heated rotating stage is used during the angular thermal emission measurements (0−70°, every 2°). The sample (heated to 266 °C) is focused by the parabolic mirror, and the infrared beam is collected through the back port of the FTIR bench. A Ge polarizer (Pike Technologies) is placed outside the FTIR bench when doing polarized (0/90° polarized) angular thermal emission measurements.

ASSOCIATED CONTENT

Supporting Information

The Supporting Information is available free of charge at https://pubs.acs.org/doi/10.1021/acsomega.0c00600.

> Reflection measurements of the SiC substrate at three elevated temperatures; two-dimensional analysis of the thermal model; angular radiation pattern of the NIREM for unpolarized emission; and details of the numerical simulations (PDF)

AUTHOR INFORMATION

Corresponding Author

Joshua D. Caldwell − *Department of Mechanical Engineering, Vanderbilt University, Nashville, Tennessee 37212, United States;* orcid.org/0000-0003-0374-2168; Email: josh.caldwell@vanderbilt.edu

Authors

Guanyu Lu − *Department of Mechanical Engineering, Vanderbilt University, Nashville, Tennessee 37212, United States;* orcid.org/0000-0001-8960-0464

Joshua Ryan Nolen − *Interdisciplinary Materials Science, Vanderbilt University, Nashville, Tennessee 37212, United States*

Thomas G. Folland − *Department of Mechanical Engineering, Vanderbilt University, Nashville, Tennessee 37212, United States;* orcid.org/0000-0002-4665-235X

Marko J. Tadjer − *US Naval Research Laboratory, Washington, Washington, D.C. 20375, United States*

Don Greg Walker − *Department of Mechanical Engineering, Vanderbilt University, Nashville, Tennessee 37212, United States*

Complete contact information is available at: https://pubs.acs.org/10.1021/acsomega.0c00600

Notes

The authors declare no competing financial interest.

ACKNOWLEDGMENTS

Research at NRL was supported by the Office of Naval Research. The authors are sincerely grateful to Milton Rebbert (NRL) for SiC wafer dicing and Ni electroplating, as well as Dr. Gerard Henein (NIST) for ion milling assistance. Fabrication at Vanderbilt, development of the variable angle thermal emission apparatus and efforts by D.G.W. and J.D.C. were supported through a Short-Term Innovative Research grant from the Army Research Office (grant number W911NF1810392). Efforts by J.R.N. was supported at Vanderbilt by the Office of Naval Research under grant (N00014-18-1-2107). G.L. and T.G.F. were both supported through Vanderbilt University via the startup package provided to J.D.C. A portion of this research was conducted at the Vanderbilt Institute of Nanoscale Science and Engineering.

REFERENCES

(1) Raman, A. P.; Anoma, M. A.; Zhu, L.; Rephaeli, E.; Fan, S. Passive radiative cooling below ambient air temperature under direct sunlight. *Nature* **2014**, *515*, 540−544.

(2) Goldstein, E. A.; Raman, A. P.; Fan, S. Sub-ambient non-evaporative fluid cooling with the sky. *Nat. Energy* **2017**, *2*, 17143.

(3) Shen, S.; Narayanaswamy, A.; Chen, G. Surface phonon polaritons mediated energy transfer between nanoscale gaps. *Nano Lett.* **2009**, *9*, 2909−2913.

(4) Kim, K.; Song, B.; Fernández-Hurtado, V.; Lee, W.; Jeong, W.; Cui, L.; Thompson, D.; Feist, J.; Reid, M. T. H.; García-Vidal, F. J.; Cuevas, J. C.; Meyhofer, E.; Reddy, P. Radiative heat transfer in the extreme near field. *Nature* **2015**, *528*, 387−391.

(5) Hodgkinson, J.; Tatam, R. P. Optical gas sensing: a review. *Meas. Sci. Technol.* **2013**, *24*, 012004.

(6) Miller, D. A. B. Attojoule Optoelectronics for Low-Energy Information Processing and Communications. *J. Lightwave Technol.* **2017**, *35*, 346−396.

(7) Greffet, J.-J.; Carminati, R.; Joulain, K.; Mulet, J.-P.; Mainguy, S.; Chen, Y. Coherent emission of light by thermal sources. *Nature* **2002**, *416*, 61−64.
(8) Schuller, J. A.; Taubner, T.; Brongersma, M. L. Optical antenna thermal emitters. *Nat. Photonics* **2009**, *3*, 658−661.
(9) Wang, T.; Li, P.; Chigrin, D. N.; Giles, A. J.; Bezares, F. J.; Glembocki, O. J.; Caldwell, J. D.; Taubner, T. Phonon-Polaritonic Bowtie Nanoantennas: Controlling Infrared Thermal Radiation at the Nanoscale. *ACS Photonics* **2017**, *4*, 1753−1760.
(10) Faist, J. Wallplug efficiency of quantum cascade lasers: Critical parameters and fundamental limits. *Appl. Phys. Lett.* **2007**, *90*, 253512.
(11) Yao, Y.; Hoffman, A. J.; Gmachl, C. F. Mid-infrared quantum cascade lasers. *Nat. Photonics* **2012**, *6*, 432.
(12) Han, S. E. Theory of thermal emission from periodic structures. *Phys. Rev. B: Condens. Matter Mater. Phys.* **2009**, *80*, 155108.
(13) Chalabi, H.; Alù, A.; Brongersma, M. L. Focused thermal emission from a nanostructured SiC surface. *Phys. Rev. B: Condens. Matter Mater. Phys.* **2016**, *94*, 094307.
(14) De Zoysa, M.; Asano, T.; Mochizuki, K.; Oskooi, A.; Inoue, T.; Noda, S. Conversion of broadband to narrowband thermal emission through energy recycling. *Nat. Photonics* **2012**, *6*, 535−539.
(15) Folland, T. G.; Nordin, L.; Wasserman, D.; Caldwell, J. D. Probing polaritons in the mid- to far-infrared. *J. Appl. Phys.* **2019**, *125*, 191102.
(16) Basov, D. N.; Fogler, M. M.; Garcia de Abajo, F. J. Polaritons in van der Waals materials. *Science* **2016**, *354*, aag1992.
(17) Low, T.; Chaves, A.; Caldwell, J. D.; Kumar, A.; Fang, N. X.; Avouris, P.; Heinz, T. F.; Guinea, F.; Martin-Moreno, L.; Koppens, F. Polaritons in layered two-dimensional materials. *Nat. Mater.* **2017**, *16*, 182−194.
(18) Landy, N. I.; Sajuyigbe, S.; Mock, J. J.; Smith, D. R.; Padilla, W. J. Perfect metamaterial absorber. *Phys. Rev. Lett.* **2008**, *100*, 207402.
(19) Vassant, S.; Hugonin, J.-P.; Marquier, F.; Greffet, J.-J. Berreman mode and epsilon near zero mode. *Opt. Express* **2012**, *20*, 23971−23977.
(20) Kelley, K. P.; Runnerstrom, E. L.; Sachet, E.; Shelton, C. T.; Grimley, E. D.; Klump, A.; LeBeau, J. M.; Sitar, Z.; Suen, J. Y.; Padilla, W. J.; Maria, J.-P. Multiple Epsilon-Near-Zero Resonances in Multilayered Cadmium Oxide: Designing Metamaterial-Like Optical Properties in Monolithic Materials. *ACS Photonics* **2019**, *6*, 1139−1145.
(21) Foteinopoulou, S.; Devarapu, G. C. R.; Subramania, G. S.; Krishna, S.; Wasserman, D. Phonon-polaritonics: enabling powerful capabilities for infrared photonics. *Nanophotonics* **2019**, *8*, 2129−2175.
(22) Caldwell, J. D.; Lindsay, L.; Giannini, V.; Vurgaftman, I.; Reinecke, T. L.; Maier, S. A.; Glembocki, O. J. Low-loss, infrared and terahertz nanophotonics using surface phonon polaritons. *Nanophotonics* **2015**, *4*, 44−68.
(23) Howes, A.; Nolen, J. R.; Caldwell, J. D.; Valentine, J. Near-Unity and Narrowband Thermal Emissivity in Balanced Dielectric Metasurfaces. *Adv. Opt. Mater.* **2019**, *8*, 1901470.
(24) Adachi, S. *Handbook on Physical Properties of Semiconductors*; Kluwer Academic Publishers: Boston, 2004; p 1−344.
(25) Caldwell, J. D.; Glembocki, O. J.; Francescato, Y.; Sharac, N.; Giannini, V.; Bezares, F. J.; Long, J. P.; Owrutsky, J. C.; Vurgaftman, I.; Tischler, J. G.; Wheeler, V. D.; Bassim, N. D.; Shirey, L. M.; Kasica, R.; Maier, S. A. Low-loss, extreme subdiffraction photon confinement via silicon carbide localized surface phonon polariton resonators. *Nano Lett.* **2013**, *13*, 3690−3697.
(26) Caldwell, J. D.; Kretinin, A. V.; Chen, Y.; Giannini, V.; Fogler, M. M.; Francescato, Y.; Ellis, C. T.; Tischler, J. G.; Woods, C. R.; Giles, A. J.; Hong, M.; Watanabe, K.; Taniguchi, T.; Maier, S. A.; Novoselov, K. S. Sub-diffractional volume-confined polaritons in the natural hyperbolic material hexagonal boron nitride. *Nat. Commun.* **2014**, *5*, 5221.
(27) Chen, Y.; Francescato, Y.; Caldwell, J. D.; Giannini, V.; Maß, T. W. W.; Glembocki, O. J.; Bezares, F. J.; Taubner, T.; Kasica, R.; Hong, M.; Maier, S. A. Spectral Tuning of Localized Surface Phonon Polariton Resonators for Low-Loss Mid-IR Applications. *ACS Photonics* **2014**, *1*, 718−724.
(28) Inoue, T.; De Zoysa, M.; Asano, T.; Noda, S. Realization of narrowband thermal emission with optical nanostructures. *Optica* **2015**, *2*, 27−35.
(29) Luna, L. E.; Tadjer, M. J.; Anderson, T. J.; Imhoff, E. A.; Hobart, K. D.; Kub, F. J. Deep reactive ion etching of 4H-SiC via cyclic SF6/O2 segments. *J. Micromech. Microeng.* **2017**, *27*, 095004.
(30) Folland, T. G.; Lu, G.; Bruncz, A.; Nolen, J. R.; Tadjer, M.; Caldwell, J. D. Vibrational Coupling to Epsilon-Near-Zero Waveguide Modes. *ACS Photonics* **2020**, *7*, 614−621.
(31) Xiao, Y.; Shahsafi, A.; Wan, C.; Roney, P. J.; Joe, G.; Yu, Z.; Salman, J.; Kats, M. A. Measuring Thermal Emission Near Room Temperature Using Fourier-Transform Infrared Spectroscopy. *Phys. Rev. Appl.* **2019**, *11*, 014026.
(32) Nakashima, S.; Harima, H. Raman Investigation of SiC Polytypes. *Phys. Status Solidi A* **1997**, *162*, 39−64.
(33) Paarmann, A.; Razdolski, I.; Gewinner, S.; Schöllkopf, W.; Wolf, M. Effects of crystal anisotropy on optical phonon resonances in midinfrared second harmonic response of SiC. *Phys. Rev. B: Condens. Matter Mater. Phys.* **2016**, *94*, 134312.

https://dx.doi.org/10.1021/acsomega.0c00600
ACS Omega 2020, 5, 10900−10908